Article

Three-Dimensional Swirling Flow of Nanofluid with Nanoparticle Aggregation Kinematics Using Modified Krieger–Dougherty and Maxwell–Bruggeman Models: A Finite Element Solution

M. D. Alsulami [1] , **Amal Abdulrahman** [2] , **R. Naveen Kumar** [3] , **R. J. Punith Gowda** [4] **and B. C. Prasannakumara** [5,*]

1   Department of Mathematics, College of Sciences and Arts at Alkamil, University of Jeddah, Jeddah 21589, Saudi Arabia; mdalsolami@uj.edu.sa
2   Department of Chemistry, College of Science, King Khalid University, Abha 61421, Saudi Arabia
3   Department of Mathematics, Dayananda Sagar College of Engineering, Bangalore 560078, India; nkrmaths@gmail.com
4   Department of Mathematics, Bapuji Institute of Engineering & Technology, Davanagere 577004, India; rjpunithgowda@gmail.com
5   Department of Studies and Research in Mathematics, Davanagere University, Davanagere 577007, India
*   Correspondence: prasannakumarabc@davangereuniversity.ac.in or dr.bcprasanna@gmail.com

Abstract: The current study explores a three-dimensional swirling flow of titania–ethylene glycol-based nanofluid over a stretchable cylinder with torsional motion. The heat transfer process is explored subject to heat source/sink. Here, titania–ethylene glycol–water-based nanofluid is used. The Maxwell–Bruggeman models for thermal conductivity and modified Krieger–Dougherty models for viscosity are employed to scrutinize the impact of nanoparticle aggregation. A mathematical model based on partial differential equations (PDEs) is developed to solve the flow problem. Following that, a similarity transformation is performed to reduce the equations to ordinary differential equations (ODEs), which are then solved using the finite element method. It has been proven that nanoparticle aggregation significantly increases the temperature field. The results reveal that the rise in Reynolds number improves the heat transport rate, whereas an increase in the heat source/sink parameter value declines the heat transport rate. Swirling flows are commonly found in many industrial processes such as combustion, mixing, and fluidized bed reactors. Studying the behavior of nanofluids in these flows can lead to the development of more efficient and effective industrial processes.

Keywords: swirling flow; stretchable cylinder; torsional motion; nanofluid; heat source/sink; nanoparticle aggregation

MSC: 65L60; 76M10

1. Introduction

Flow over rotating and stretching cylinders is vital in a wide range of uses, including axles and shafts, as well as spinning projectiles. When referring to the motion of a fluid, the term "swirling flow" refers to a motion in which the velocity vector of the liquid particle spins around a central axis, producing a pattern that resembles a vortex or spiral. This form of flow may be seen in many natural phenomena, such as whirlpools, tornadoes, and hurricanes, as well as in many industrial processes. The three-dimensional swirling flow can be used in microfluidic devices for mixing and separating particles or cells. Numerous researchers have recently used computational, theoretical, and experimental methods to investigate the incompressible flow around a spinning circular cylinder. Aerodynamic difficulties and engineering constructions are two areas where this field has many applications.

Wang's [1] pure stretching motion of a cylinder was substituted with a pure torsional motion by Sprague and Weidman [2]. They radially entrained flow at high Reynolds numbers and compared them to comprehensive numerical data attained over a varied Reynolds number. The cylindrical coordinates (r, θ, z) were naturally used, with the appropriate coordinate velocities denoted as (u, v, w). The flow outside the cylinder in Wang's issue was driven by the cylinder surface's linear axial stretching $w = kz$. The impact of heat generation/absorption on Casson fluid stream across a swirling cylinder was discussed by Javed et al. [3]. In this study, the researchers came to the conclusion that the magnitude of axial skin friction increases with a bigger Reynold number and magnetic parameter. The stream of the Maxwell liquid around an elastic spinning cylinder with torsional motion was conferred by Khan et al. [4]. Their findings indicated that the velocity decreased at a rate proportional to the square of the Reynolds number and decreased as the Reynolds number increased. Additionally, the stream penetrated less deeply inside the free stream liquid. Ahmed et al. [5] used a flexible cylinder with whirling to examine the thermal properties of a hybrid nanofluid stream. According to the findings, the temperature of the fluid was shown to decline in a manner exponentially proportional to increasing values of the Reynolds number.

Over past decades, the heat transfer improvement has received considerable attention, due to its significance in engineering and manufacturing applications. Most engineering apparatuses, such as electronic devices and heat exchangers, traditionally employ heat transport fluids such as ethylene glycol (EG), water, and oil. However, because these carrier liquids have a low thermal conductivity, the heat transport increase is limited. Thermal scientists have enhanced the aforementioned liquids by adding a single type of nanosized particle to create a combination known as a nanofluid (NF), which was initially developed by Choi. Nanoparticles (NPs) have been shown in studies to have exceptional potential for increasing the heat transport rate and thermal conductivity of base liquids. Since then, many studies have emphasized the heat transport of an NF for various features, either experimentally or mathematically. Ali et al. [6] conferred the flow and heat transport of the NF in a circular microchannel heat sink using swirl condition. Rafiq and Mustafa [7] conferred the flow of NF over a disc by considering six different NPs. The findings demonstrated that suction seems to play a critical role in enhancing heat transport of the working liquid of NPs, similar to the steady-state situation. Usman et al. [8] inspected the radiative cross-NF stream over a swirling surface using the Buongiorno NF model. According to their findings, the radial velocity of the two discs increased when their respective ratio stretching rate parameters were increased, but went down when the Rayleigh number and the Hall parameter increased. Reddy et al. [9] determined the consequence of the chemical reaction on the single-phase NF heat and mass transport features. Variations in the scatterings of swirling velocity, axial velocity, concentration, and temperature with numerous relevant factors were depicted via plots. These variations were shown to exist as a consequence of the findings. The hydrothermal characteristics of two hybrid NFs and a conventional NF were investigated by Gangadhar et al. [10] using a stretchable swirling cylinder as the experimental setup. In this part of the paper, they said that every highest competent finite element technique was implemented by removing subsequent equations and boundary constraints. The validity and trustworthiness of the current numerical explanation are remarkable, because it is in wonderful harmony with existing answers that are straightforward in the literature.

Aggregation can have significant effects on the properties and performance of nanoparticles, such as altering their size, shape, and surface area, and reducing their effectiveness in applications. Therefore, it is important to understand and control nanoparticle aggregation to achieve the desired outcomes. NPs with a much smaller size and greater surface area have the ability to considerably improve heat transmission and fluid stability. Experiments have further shown that aggregation of NPs has a big influence on thermal and rheological properties. The van der Waals force and surface charge cause NPs to form groups. Linear chains and percolating networks are formed by these NPs, making it easier for heat to

pass through them. Heat flows faster in the aggregation of NPs than it does in NPs. The nanoparticle aggregation kinematics can be used to control the motion of nanoparticles in the microfluidic channels. Aggregation of the metallic oxide NPs with a variety of pH values in order to increase the thermal conductivity was investigated by Wensel [11], using two different modified versions, the Krieger–Dougherty and the Maxwell–Bruggeman types. Using the Maxwell–Garnett model, Prasher et al. [12] investigated the trigger of aggregations kinetics of heat transmission for a nano suspension solution and its unique function via experimental data. The stimulant of the aggregation effect of NF with porosity was investigated by Ellahi et al. [13]. Zhoe et al. [14] conducted research on the NEMD simulation and compared the outcomes of their findings related to the thermal energy features of aggregation of nanoparticles. The contribution of Kapitza conductance of nanosized particles and water was reported and compared by Roodbari et al. [15] in conjunction with the particles' surface wettability and diameter. Alzahrani et al. [16] studied the impact of NP aggregation on Oldroyd-B NF. The investigation's findings indicated that the case of liquid flow with NP aggregation demonstrated increased heat transfer in comparison to improved heat source/sink parameter values. The influence of NP aggregation and other influencing factors on the NF stream on different surfaces was investigated by Wang et al. [17,18]. The findings indicated that the heat transfer efficiency in the case of flow dynamics with NP aggregation was enhanced for higher values of the radiation parameter. Moreover, the study of the flow of fluid with aggregation revealed a rise in the heat transport rate at the surface of a cone as the radiation parameter values were elevated. Mahanthesh et al. [19] investigated the heat transport of NPs in the presence of NP aggregation. The findings indicated that the erratic motion and thermophoretic migration of NPs resulted in an increase in the thickness of the thermal boundary layer. Yu et al. [20] investigated the particle deposition influence on the stream of a micropolar NF. The results indicated that the presence of NP aggregation had a reduced effect on the velocity field, but a more significant effect on the mass and heat transport.

Fluid flow with a heat source/sink (HSS) refers to the flow of a fluid that is accompanied by the transfer of heat due to the presence of a heat source or sink. This type of flow is commonly encountered in various engineering applications, such as cooling of electronic components, heat exchangers, and geothermal systems. The use of nanofluids in flow with HSS applications has the potential to improve heat transfer efficiency and reduce energy consumption in various industrial processes. The effects of an HSS on rate type NF flow were discussed by Muthucumaraswamy and Sivakumar et al. [21]. The melting impact on a Cu–Fe_2SO_4–H_2O hybrid NF with HSS was studied by Radhika et al. [22]. The findings indicated that the enhancement of heat transport rate was attributed to the increase in thermal conductivity and HSS parameter. Faisal et al. [23] described the flow of an NF on a surface with HSS. The authors employed the grid independence methodology to validate the convergence of the numerical solution. Additionally, the computational time was measured to assess the efficacy of the numerical scheme utilized for solution determination. Chu et al. [24] explained the HSS characteristics of the Rabinowitsch liquid using a circular tube. The findings indicated that the enhancement of heat transport rate through a tube was attributed to the increase in thermal conductivity and HSS parameter. Gowda et al. [25] investigated the HSS and radiation effects on the second-grade liquid stream across a plate. The results indicated that an increase in HSS and radiation parameters led to enhanced heat transport.

On the basis of the literature review presented above, this study aimed to investigate the effect of a heat source/sink (HSS) on the flow of a nanofluid over a swirling cylinder with torsional motion, taking into account the aggregation of nanoparticles (NPs), which represents the novelty of this work. To the best of our knowledge, no prior study has defined an NF model for fluid flow with HSS and torsional motion. Therefore, the mathematical formulation presented in this study is original and has not been discussed before. The main objective of this study was to fill this research gap by conducting a heat transport analysis of the NF flow, answering the following research questions:

- ❖　What effect does the Reynolds number have on flow and heat transport behavior?
- ❖　What is the impact of the dimensionless heat source/sink parameter on the thermal profiles of an NF with and without NP aggregation?
- ❖　What impact does an increase in Reynolds number and heat source/sink parameter have on the rate of heat transfer?
- ❖　What impact does an increase in Reynolds number and heat source/sink parameter have on heat transfer in an NF with and without NP aggregation?

2. Problem Formulation

Consider a three-dimensional, steady, laminar, swirling flow of a titania–EG NF over a stretchable cylinder with a torsional motion. The heat transfer process subject to HSS is explored. The Maxwell–Bruggeman models for thermal conductivity and modified Krieger–Dougherty models for viscosity are employed to scrutinize the impact of NP aggregation. The flow geometry is presented in Figure 1.
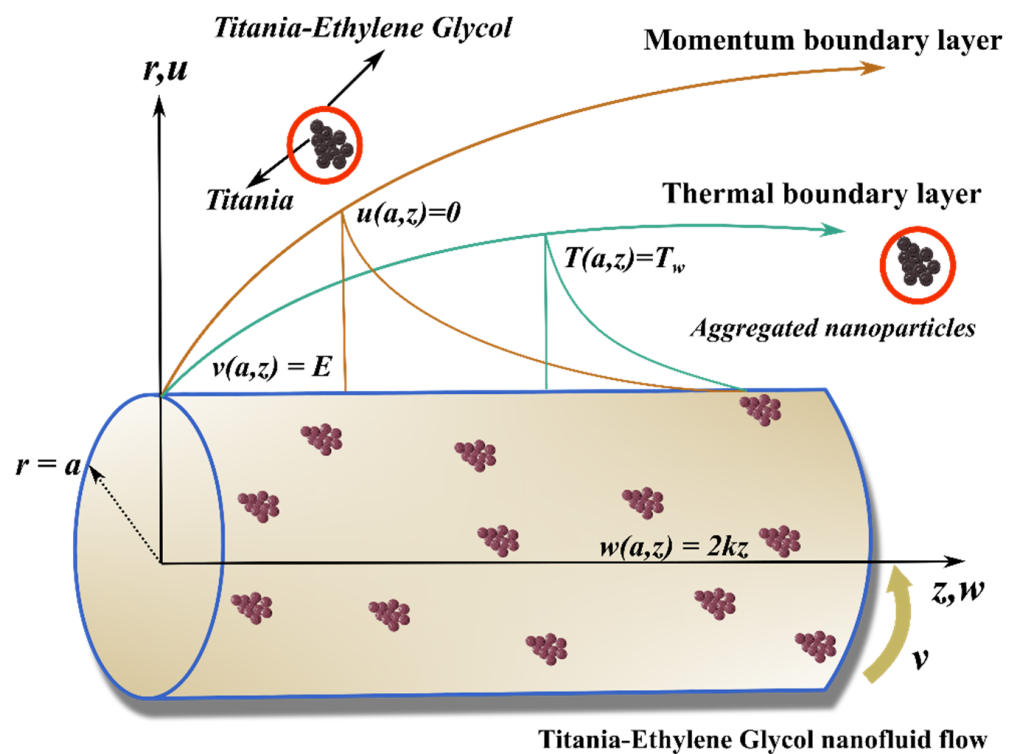
Figure 1. Physical description of flow problem.

2.1. Assumptions and Conditions of the Model

The mathematical model is considered under the following assumptions and conditions:

- ❖　Three-dimensional laminar flow,
- ❖　The Maxwell–Bruggeman models for thermal conductivity,
- ❖　The modified Krieger–Dougherty models for viscosity,
- ❖　NP aggregation,
- ❖　Titania–EG NF,
- ❖　Swirling flow,
- ❖　Stretching cylinder with a torsional motion.

2.2. Geometry of Fluid Flow

The geometry of the flow model is given below.

2.3. Model Equation

For incompressible fluids based on the axisymmetric flow assumption and without body force, the Navier–Stokes equation in cylindrical coordinates for the system under consideration is expressed as follows [26]:

$$(ur)_r + (wr)_z = 0,$$ (1)

$$u_r u + u_z w - \frac{v^2}{r} = -\frac{p_r}{\rho_{nf}} + v_{nf}\left(u_{zz} - \frac{1}{r^2}u + \frac{1}{r}u_r + u_{rr}\right),$$ (2)

$$v_r u + v_z w + \frac{vu}{r} = v_{nf}\left(v_{zz} - \frac{1}{r^2}v + \frac{1}{r}v_r + v_{rr}\right),$$ (3)

$$w_r u + w_z w = -\frac{p_z}{\rho_{nf}} + v_{nf}\left(w_{zz} + \frac{1}{r}w_r + w_{rr}\right),$$ (4)

$$uT_r + wT_z = \alpha_{nf}\left(T_{rr} + \frac{T_r}{r} + T_{zz}\right) + \frac{Q_0}{(\rho C_p)_{nf}}(T - T_\infty),$$ (5)

with the corresponding boundary constraints

$$\begin{aligned} w(a,z) &= 2Kz, u(a,z) = 0, T(a,z) = T_w, v(a,z) = E, \\ w(\infty,z) &\to 0, v(\infty,z) \to 0, T(\infty,z) \to 0. \end{aligned}$$ (6)

It is assumed that the flow is caused solely by the stretching of the surface with the free stream velocity being zero. The controlling boundary layer equations are reduced to ODEs using the following collection of similarity transformations:

$$v = Eg(\eta), \theta(\eta) = \frac{T - T_\infty}{T_w - T_\infty}, u = -Ka\frac{f(\eta)}{\sqrt{\eta}}, w = 2Kzf'(\eta), \eta = \frac{r^2}{a^2}.$$ (7)

2.4. Thermo-Physical and Thermal Characteristics for Aggregation Process

The following are the effective density, viscosity, heat capacitance, and thermal conductivity of nanofluid for nanoparticle aggregation [27–29]:

$$\mu_{nf} = \mu_f\left(1 - \frac{\phi_{agg}}{\phi_{max}}\right)^{-2.5*\phi_{max}},$$ (8)

$$\phi = \phi_{agg}\phi_{int}, \phi_{int} = \left(\frac{R_{agg}}{R_p}\right)^{D-3},$$ (9)

$$\rho_{nf} = \phi_{agg}\rho_{agg} + \rho_f(1 - \phi_{agg}),$$ (10)

$$\rho_{agg} = (1 - \phi_{int})\rho_f + \phi_{int}\rho_s,$$ (11)

$$(\rho C_p)_{nf} = (1 - \phi_{agg})(\rho C_p)_f + \phi_{agg}(\rho C_p)_{agg},$$ (12)

$$(\rho C_p)_{agg} = (1 - \phi_{int})(\rho C_p)_f + \phi_{int}(\rho C_p)_s,$$ (13)

$$k_{nf} = k_f\left(\frac{k_{agg} + 2k_f + 2\phi_{agg}(k_{agg} - k_f)}{k_{agg} + 2k_f - \phi_{agg}(k_{agg} - k_f)}\right),$$ (14)

$$k_{agg} = \frac{k_f}{4} \left(\begin{array}{c} [3\phi_{\text{int}} - 1]\frac{k_s}{k_f} + [3(1 - \phi_{\text{int}}) - 1]+ \\ \left[\left[(3\phi_{\text{int}} - 1)\frac{k_s}{k_f} + (3(1 - \phi_{\text{int}}) - 1) \right]^2 + \frac{8k_s}{k_f} \right]^{\frac{1}{2}} \end{array} \right) \tag{15}$$

Considering the spherical aggregation, fractal index D takes the value of 1.8, $\frac{R_{agg}}{R_p} = 3.34$, and $\phi_{\max} = 0.605$. To precisely evaluate the effective thermal conductivity of $TiO_2 - EG$ NF, the more realistic Maxwell and Bruggeman framework is intended. Table 1 displays the thermophysical properties of NPs and the base liquid.

Table 1. Thermophysical properties of NPs and the base liquid [29].

	μ (kg m^{-1}s^{-1})	C_p(Jkg^{-1}K^{-1})	k(WmK^{-1})	ρ(kgm^{-3})
Ethylene glycol	0.0157	2415	0.252	1114
TiO$_2$	−	686.2	8.9538	4250

2.5. Reduced Equations and Expressions for Parameters

The equations are reduced as follows by using similarity transformation Equation (7) along with the effective density, viscosity, heat capacitance, and thermal conductivity of the nanofluid for nanoparticle aggregation (Equations (8)–(13)):

$$(\eta \aleph_1 f''' + \aleph_1 f'') + \text{Re}\left(f f'' - f'^2 \right) = 0, \tag{16}$$

$$\left(\eta \aleph_1 g'' - \aleph_1 \frac{g}{4\eta} + \aleph_1 g' \right) + \left(\text{Re} g' f - \frac{\text{Re}}{2} \frac{gf}{\eta} \right) = 0, \tag{17}$$

$$\frac{1}{\text{Pr}} \frac{k_{nf}}{k_f} \left(\aleph_2 \eta \theta'' + \aleph_2 \theta' \right) + \text{Re} f \theta' + \text{Re} \aleph_2 Q \theta = 0. \tag{18}$$

Here,

$$\aleph_1 = \frac{\nu_{nf}}{\nu_f}, \quad \frac{1}{\aleph_2} = \frac{(\rho C_p)_{nf}}{(\rho C_p)_f}.$$

The corresponding BCs are

$$\begin{array}{c} g(\infty) \to 0; g(1) = 1; \theta(1) = 1; f(1) = 0; \\ f'(\infty) \to 0; f'(1) = 1; \theta(\infty) \to 0. \end{array} \tag{19}$$

The involved nondimensional parameters in the flow problem are

$$\text{Re} = \frac{Ka^2}{2\nu_f}, Q = \frac{Q_0}{2K(\rho C_p)_f}, \text{Pr} = \frac{\mu_f (C_p)_f}{k_f}.$$

2.6. Quantities for Engineering Interest

Another object of this problem is to calculate skin friction coefficients along the swirling and radial directions, as well as the Nusselt number, which are given as

$$\begin{array}{c} \text{Re} C_{fs} = (2\aleph_3 g'(1) - \aleph_3 g(1)), \\ \text{Re} C_{fx} = \aleph_3 f''(1), \\ \frac{Nu}{\text{Re}^{\frac{1}{2}}} = -\frac{k_{nf}}{k_f} \theta'(1). \end{array} \tag{20}$$

Here,

$$\frac{1}{\aleph_3} = \frac{\mu_f}{\mu_{nf}}.$$

3. Finite Element Method Solutions

The finite element method (FEM) is a numerical approach that is used to estimate solutions to differential equations in various areas, such as engineering, physics, and applied mathematics. The FEM is frequently utilized when analytical solutions are not readily available for issues involving complicated geometries or boundary conditions. In addition to this, it is able to deal with issues that involve nonlinearities and time-dependent phenomena. The FEM may be utilized in a variety of contexts, such as in the fields of structural analysis, fluid dynamics, heat transfer, and electromagnetics (see [30–34]). The finite element method (FEM) has been utilized to solve the system of ODEs (Equations (16–18)) with boundary constraints (Equation (19)). This technique is potent for solving PDEs and ODEs. When compared to several other numerical methods, the FEM is most reliable and capable. The FEM solves BVPs precisely, rapidly, and adequately. FEM includes continuous piecewise approximation, which minimizes the size of error. Initially, we assume

$$f' = H. \tag{21}$$

The system of equations can be transformed to lower order as follows:

$$\aleph_1 \left(\eta H'' + H' \right) + \mathrm{Re} \left(H'f - H^2 \right) = 0, \tag{22}$$

$$\eta g'' + \mathrm{Re} g'f - \aleph_1 \frac{g}{4\eta} - \frac{\mathrm{Re}}{2} \frac{gf}{\eta} + \aleph_1 g' = 0, \tag{23}$$

$$\frac{1}{\mathrm{Pr}} \frac{k_{nf}}{k_f} \left(\eta \theta'' + \theta' \right) \aleph_2 + \mathrm{Re} f \theta' + \mathrm{Re} \aleph_2 Q \theta = 0, \tag{24}$$

along with the following boundary constraints:

$$f(1) = 0; H(1) = 1; \theta(1) = 1; H(\infty) \to 0; g(1) = 1; g(\infty) \to 0; \theta(\infty) \to 0. \tag{25}$$

The variational form connected with the above reduced smaller-order equations over a typical element (η_e, η_{e+1}) can be described as

$$\int_{\eta_e}^{\eta_{e+1}} h_1 \left(f' - H \right) d\eta = 0,$$

$$\int_{\eta_e}^{\eta_{e+1}} h_2 \left[\aleph_1 \left(\eta H'' + H' \right) + \mathrm{Re} \left(H'f - H^2 \right) \right] d\eta = 0,$$

$$\int_{\eta_e}^{\eta_{e+1}} h_3 \left(\eta g'' + \mathrm{Re} g'f - \aleph_1 \frac{g}{4\eta} - \frac{\mathrm{Re}}{2} \frac{gf}{\eta} + \aleph_1 g' \right) d\eta = 0,$$

$$\int_{\eta_e}^{\eta_{e+1}} h_4 \left(\frac{1}{\mathrm{Pr}} \frac{k_{nf}}{k_f} \left(\eta \theta'' + \theta' \right) \aleph_2 + \aleph_2 \mathrm{Re} Q \theta + \mathrm{Re} f \theta' \right) d\eta = 0,$$

where h_1, h_2, h_3 and h_4 are arbitrary trial functions and may be regarded as the variation in f, H, g, and θ respectively.

The finite-element approximations are considered in the form

$$f = \sum_{j=1}^{2} f_j \Im_j, \; H = \sum_{j=1}^{2} H_j \Im_j, \; g = \sum_{j=1}^{2} g_j \Im_j, \; \text{and } \theta = \sum_{j=1}^{2} \theta_j \Im_j.$$

In this approximation, $h_1 = h_2 = h_3 = h_4 = \Im_i$ where, i $= 1, 2, 3$ and 4.

Here, shape functions $\Im_i$ are defined as

$$\Im_1^e = \frac{(\eta_e + \eta_{e+1} - 2\eta) \times (\eta_{e+1} - \eta)}{(\eta_{e+1} - \eta_e)^2},$$

$$\Im_2^e = \frac{(\eta_e - \eta) \times 4 \times (\eta - \eta_{e+1})}{(\eta_{e+1} - \eta_e)^2},$$

$$\Im_3^e = \frac{(\eta - \eta_e) \times (-2\eta + \eta_e + \eta_{e+1})}{(\eta_{e+1} - \eta_e)^2},$$

where $\eta_e \leq \eta \leq \eta_{e+1}$.

Thus, we obtain the FEM as

$$[\vartheta^e][Y^e] = [\varpi^e],$$

where ϑ represents the stiffness matrix, Y represents the vector of elemental nodal variables, and ϖ represents the force vector.

Now,

$$[\vartheta^e] = \begin{bmatrix} [\vartheta^{11}] & [\vartheta^{12}] & [\vartheta^{13}] & [\vartheta^{14}] \\ [\vartheta^{21}] & [\vartheta^{22}] & [\vartheta^{23}] & [\vartheta^{24}] \\ [\vartheta^{31}] & [\vartheta^{32}] & [\vartheta^{33}] & [\vartheta^{34}] \\ [\vartheta^{41}] & [\vartheta^{42}] & [\vartheta^{43}] & [\vartheta^{44}] \end{bmatrix}, \ [Y^e] = \begin{bmatrix} \{f\} \\ \{H\} \\ \{g\} \\ \{\theta\} \end{bmatrix}, [\varpi^e] = \begin{bmatrix} \{R^1\} \\ \{R^2\} \\ \{R^3\} \\ \{R^4\} \end{bmatrix}.$$

Here, matrices $[\vartheta^{mn}]$ and $[R^m]$ with, $m = 1, 2, 3, 4 = n$ are defined as

$$\vartheta_{ij}^{11} = \int_{\eta_e}^{\eta_{e+1}} \Im_i \frac{\partial \Im_j}{\partial \eta} d\eta, \ \vartheta_{ij}^{12} = -\int_{\eta_e}^{\eta_{e+1}} \Im_i \Im_j d\eta, \ \vartheta_{ij}^{13} = \vartheta_{ij}^{14} = \vartheta_{ij}^{21} = 0,$$

$$\vartheta_{ij}^{22} = -\aleph_1 \eta \int_{\eta_e}^{\eta_{e+1}} \frac{\partial \Im_i}{\partial \eta} \frac{\partial \Im_j}{\partial \eta} d\eta + \mathrm{Re} \int_{\eta_e}^{\eta_{e+1}} \Im_i \bar{f} \frac{\partial \Im_j}{\partial \eta} d\eta + \aleph_1 \int_{\eta_e}^{\eta_{e+1}} \Im_i \frac{\partial \Im_j}{\partial \eta} d\eta - \mathrm{Re} \int_{\eta_e}^{\eta_{e+1}} \Im_i \bar{h} \Im_j d\eta, \ \vartheta_{ij}^{23} = 0 = \vartheta_{ij}^{24},$$

$$\vartheta_{ij}^{31} = 0 = \vartheta_{ij}^{32},$$

$$\vartheta_{ij}^{33} = = -\aleph_1 \eta \int_{\eta_e}^{\eta_{e+1}} \frac{\partial \Im_i}{\partial \eta} \frac{\partial \Im_j}{\partial \eta} d\eta + \mathrm{Re} \int_{\eta_e}^{\eta_{e+1}} \Im_i \bar{f} \frac{\partial \Im_j}{\partial \eta} d\eta - \frac{\aleph_1}{4\eta} \int_{\eta_e}^{\eta_{e+1}} \Im_i \Im_j d\eta + \aleph_1 \int_{\eta_e}^{\eta_{e+1}} \Im_i \frac{\partial \Im_j}{\partial \eta} d\eta - \mathrm{Re} \int_{\eta_e}^{\eta_{e+1}} \Im_i \bar{f} \Im_j d\eta,$$

$$\vartheta_{ij}^{34} = 0,$$

$$\vartheta_{ij}^{41} = 0, \ \vartheta_{ij}^{42} = 0, \ \vartheta_{ij}^{43} = 0,$$

$$\vartheta_{ij}^{44} = -\frac{k_{nf}}{k_f} \frac{1}{\mathrm{Pr}} \aleph_2 \eta \int_{\eta_e}^{\eta_{e+1}} \frac{\partial \Im_i}{\partial \eta} \frac{\partial \Im_j}{\partial \eta} d\eta + \mathrm{Re} \int_{\eta_e}^{\eta_{e+1}} \Im_i \bar{f} \frac{\partial \Im_j}{\partial \eta} d\eta + \frac{k_{nf}}{k_f} \frac{1}{\mathrm{Pr}} \aleph_2 \int_{\eta_e}^{\eta_{e+1}} \Im_i \frac{\partial \Im_j}{\partial \eta} d\eta + \aleph_2 Q \mathrm{Re} \int_{\eta_e}^{\eta_{e+1}} \Im_i \Im_j d\eta,$$

$$R_i^1 = 0, \ R_i^2 = -\eta \aleph_1 \left[\Im_i \frac{\partial H}{\partial \eta} \right]_{\eta_e}^{\eta_{e+1}}, \ R_i^3 = -\eta \aleph_1 \left[\Im_i \frac{\partial g}{\partial \eta} \right]_{\eta_e}^{\eta_{e+1}}, \ R_i^4 = -\frac{k_{nf}}{k_f} \frac{1}{\mathrm{Pr}} \aleph_2 \eta \left[\Im_i \frac{\partial \theta}{\partial \eta} \right]_{\eta_e}^{\eta_{e+1}}.$$

4. Code Validation

The comparative analysis (code validation) helps to validate that the data presented are correct. By referring to previously published research, the current numerical approach is demonstrated to be accurate for some reduced cases (see Tables 2 and 3).

Table 2. Comparison of current results of $g'(1)$ for some reduced cases.

Re	$g'(1)$		
	Khan et al. [4]	**Fang and Yao [26]**	**Current Study**
10	-1.810074	-1.81006	-1.810061
5	-1.297884	-1.29788	-1.297862
1	-0.687943	-0.68772	-0.687931
0.5	-0.585714	-0.58488	-0.585692
0.1	-0.510233	-0.51019	-0.510195

Table 3. Comparison of current results of $f''(1)$ for some reduced cases.

Re	$f''(1)$		
	Khan et al. [4]	**Fang and Yao [26]**	**Current Study**
10	-3.344542	-3.34446	-3.344535
5	-2.417984	-2.41743	-2.417974
1	-1.179549	-1.17775	-1.179541
0.5	-0.887010	-0.88220	-0.886901
0.1	-0.489603	-0.48180	-0.489592

5. Results and Discussion

This section analyzes the impact of a variety of significant parameters on individual profiles. To better understand the behavior of the model, nonlinear ODEs are solved using the FEM technique. The act of the fascinating limits on the involved flow profiles are analyzed by means of graphs. This investigation looks at two circumstances: (a) without aggregation ($\phi_{int} = 1$ dashed lines in the figures), and (b) with aggregation ($\phi_{int} \neq 1$ solid lines in the figures). Although the similarity simulated equation group is theoretically true for positive values, the stream may become turbulent for very high values of Re; hence, the present study is only relevant for a restricted range of the Re. The flowchart of the considered problem is shown in Figure 2.

5.1. Influence of Re on Velocity Fields

The effect of Re on $f'(\eta)$ is presented in Figure 3 for two different situations, with and without NP aggregation. Here, the increased Re value reduces $f'(\eta)$ for both the flow cases. Larger Re values increase the system's inertial force, which competes with the liquid accelerating force. The flow field is reduced as a result of this logic. Moreover, the $f'(\eta)$ for flow without aggregation declines faster than the other case. The effect of Re on $g(\eta)$ is displayed in Figure 4. Here, the increased Re reduces the $g(\eta)$. There is a consistent and unchanging decline in swirling velocity, all the way down to zero as η increases. When the Reynolds number is low, the flow decays to the surrounding environment gradually, but the motion of the fluid can still penetrate relatively deeply into the ambient fluids. On the other hand, when the Reynolds number is high, the flow swirl motion diminishes quickly, and the region near the wall is the only place where fluid motion takes place. Here, it was observed that the axial velocity decreases gradually. When the Re is big enough, these algebraic deteriorating velocity profiles become exponential deteriorating profiles. Moreover, the $g(\eta)$ for flow without aggregation declines faster than the other case. Furthermore, these results agree with Khan et al. [4].
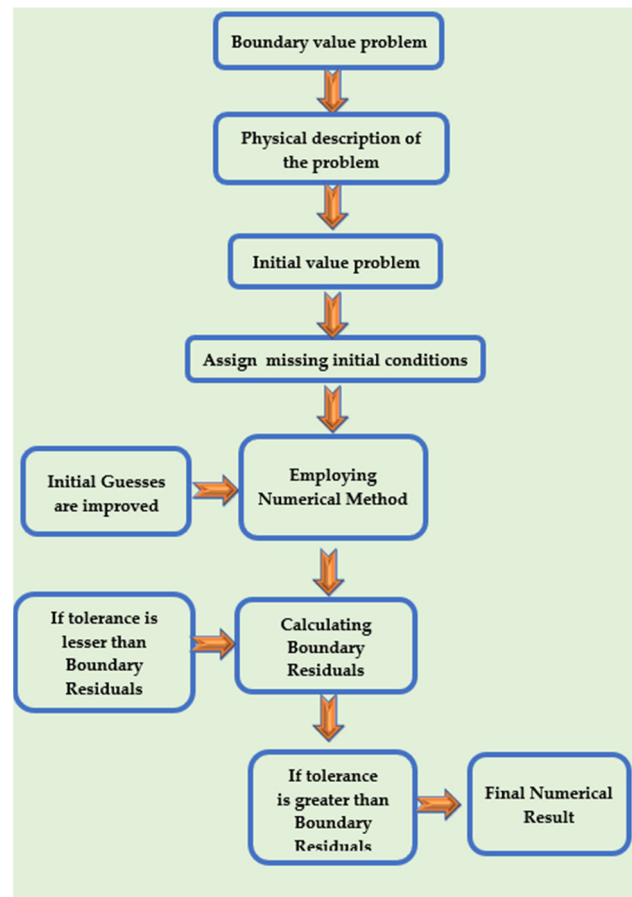
Figure 2. Flowchart of the considered problem.
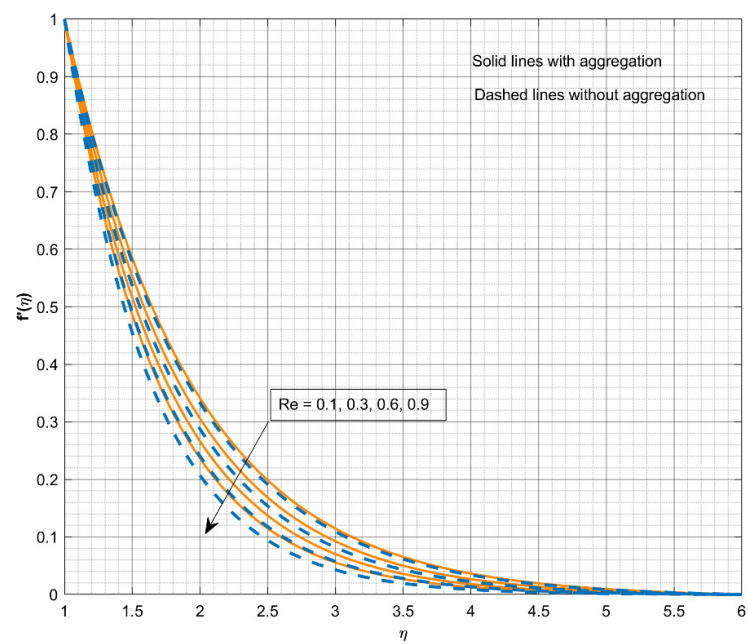
Figure 3. The impact of Re on $f'(\eta)$.
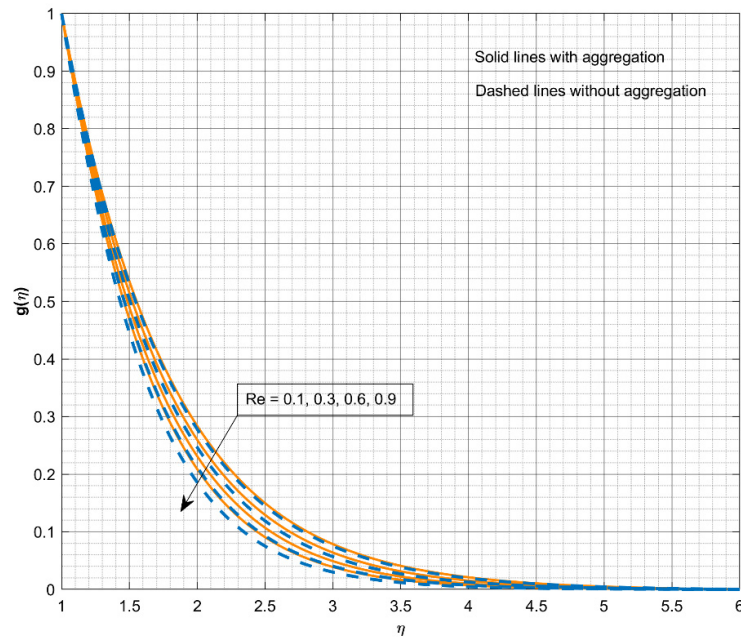
Figure 4. The impact of Re on $g(\eta)$.

5.2. Influence of Re and Q on Thermal Field

The influence of Q on $\theta(\eta)$ is portrayed in Figure 5. Here, the $\theta(\eta)$ is improved for upward Q. When there is a lower amount of heat absorption, an increase in temperature is seen in the field. With higher levels of $Q > 0$, it was discovered that the layer related to $\theta(\eta)$ produces energy, causing $\theta(\eta)$ to rise. A gradual increase in the heat source parameter results in an increase in the thickness of the thermal boundary layer. This physically reveals the fact that an increase in the heat source/sink parameter results in an increase in the amount of heat generated within the boundary layer, which in turn results in a higher temperature field. Lastly, the NF with NP aggregation shows improved heat transport compared to the other case.
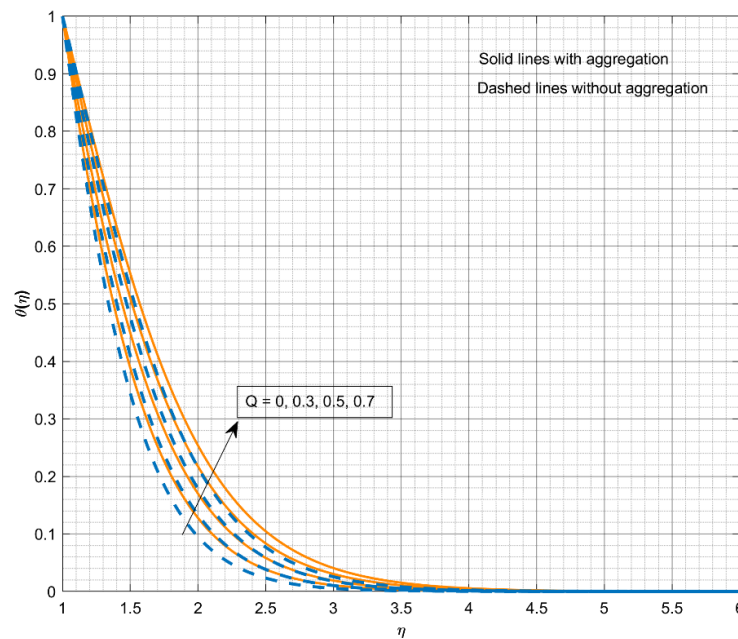
Figure 5. The impact of Q on $\theta(\eta)$.

The behavior of $\theta(\eta)$ with respect to varied Re is displayed in Figure 6. The $\theta(\eta)$ declines for improved values of Re. The Re controls liquid flow physically, and higher Re values clearly limit the stream field. As a result, the primary energy transfer method, i.e., the forced convection is diminished. The ratio of the inertial force to the viscous force is the value known as the Reynolds number. As the values of the Reynolds number are increased, the viscous force is decreased, and there is less interaction between the molecules of the fluid. For this reason, the temperature field declines. Lastly, the NF with NP aggregation shows improved heat transport compared to the other case. These results agree with Khan et al. [4].
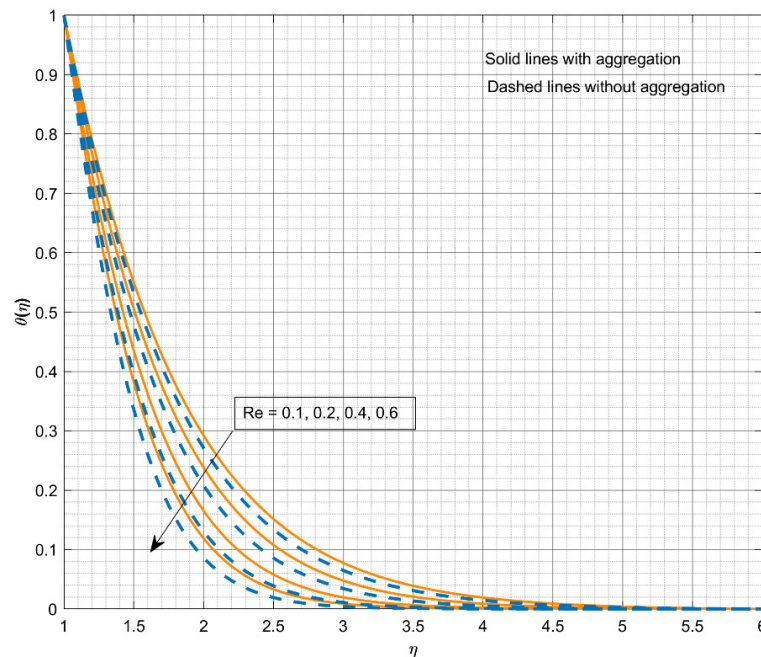
Figure 6. The impact of Re on $\theta(\eta)$.

5.3. Influence of Different Parameters on C_{fx} and $Re^{-\frac{1}{2}}Nu$

The effect of ϕ_{int} on C_{fx} versus Re is exposed in Figure 7. Here, the increment in values of ϕ_{int} advances the C_{fx}, but Re has a negative impact on it. The impact of ϕ_{int} on C_{fs} versus Re is shown in Figure 8. Here, the increment in values of ϕ_{int} augments C_{fs}, but Re has a negative impact on it. An increase in volume fraction value increases the boundary thickness, which reduces the moment of the fluid and declines the surface drag force. The effect of N_t on $Re^{-\frac{1}{2}}Nu$ versus Q is presented in Figure 9. Here, the augmentation in values of Re improves the heat transport rate, but an increment in Q value declines the heat transport rate. Moreover, the NF flow with aggregation displays enhanced heat conveyance compared to the case without aggregation. During operation, electronic equipment produces heat, and effective thermal management is essential for its dependable and secure functioning. To maximize their functionality and guarantee efficient heat dissipation, the obtained condition may be implemented in the design of cooling systems for electrical equipment, such as heat sinks and heat pipes.
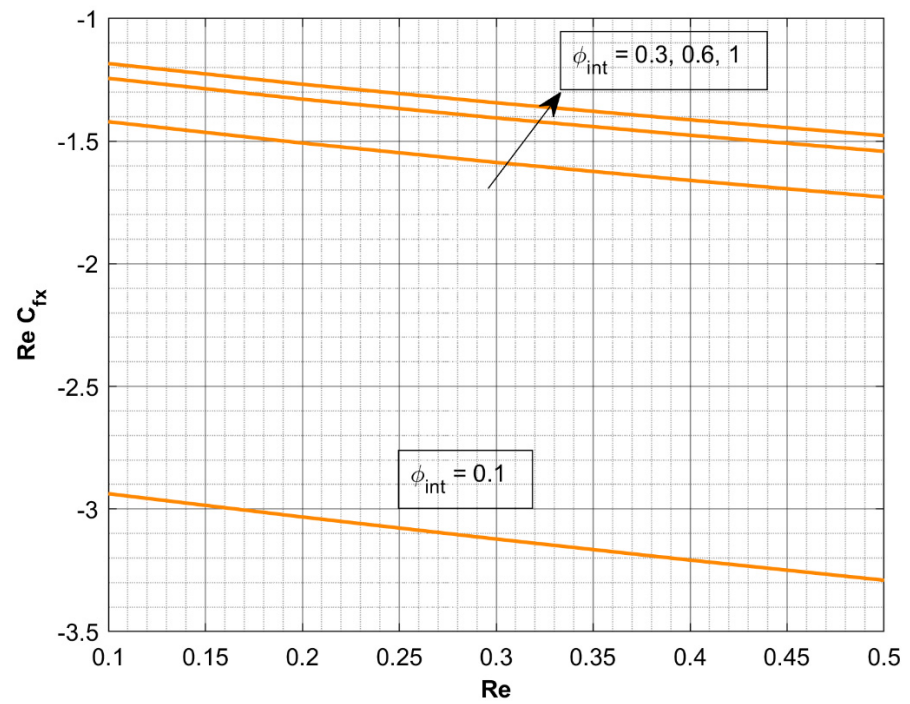
Figure 7. The impact of ϕ_{int} on $C_{fx}\text{Re}$.
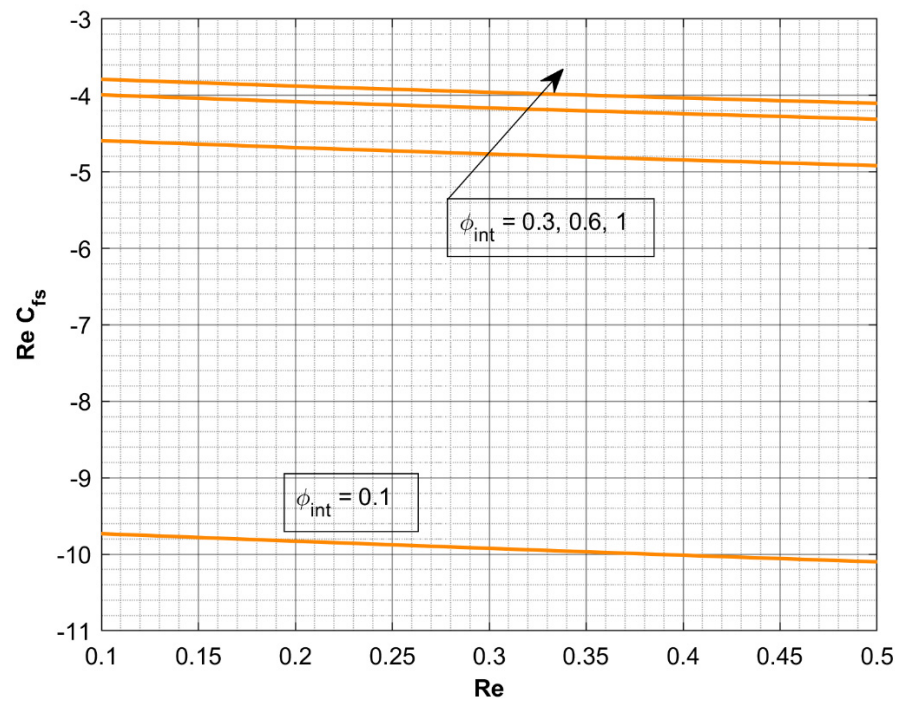
Figure 8. The impact of ϕ_{int} on $C_{fs}\text{Re}$.
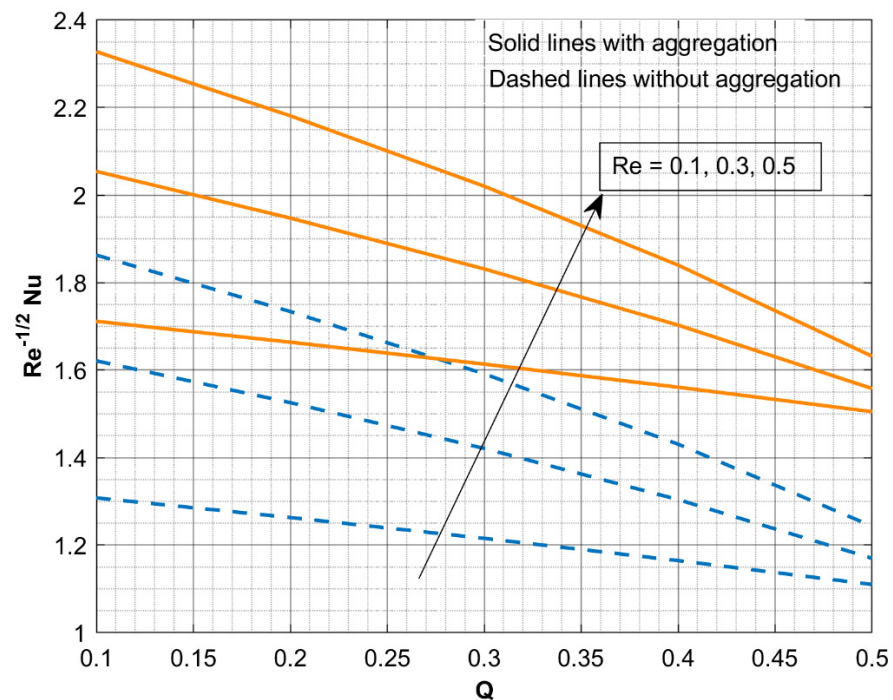
Figure 9. The impact of Re on $\mathrm{Re}^{-\frac{1}{2}}Nu$ versus Q.

6. Conclusions

A three-dimensional swirling flow of a titania–EG-based NF over a stretchable cylinder with torsional motion was investigated in this study. The heat transfer process was explored subject to HSS. Stretchable cylinders are often used in biomedical engineering applications, such as in the design of prosthetics and other medical devices. Understanding the behavior of nanofluids in swirling flow across a stretchable cylinder might give useful insights into the heat transfer properties of these fluids. This information may be helpful in the design of heat exchanging systems, as well as other types of thermal systems. The Maxwell–Bruggeman models for thermal conductivity and modified Krieger–Dougherty models for viscosity were employed to scrutinize the impact of nanoparticle aggregation. The similarity transformation was used to reduce PDEs into ODEs. This model's numerical computation was calculated using FEM. The following are the conclusions of the present study:

➢ Larger Re values enhance the system's inertial force, which resists the liquid accelerating force and declines both velocities and heat transport. This condition may be used to explore the behavior of liquids or gases in systems where inertia plays a substantial role, such as in large-scale pipelines, channels, or manufacturing processes that include the motion of liquids.

➢ The NF flow with NP aggregation shows improved heat transport compared to the other case for increased Re values.

➢ The NF with NP aggregation shows improved heat transport compared to the other case for increased Q values.

➢ The augmentation in Re advances the heat conveyance rate, but an increment in Q value declines the heat transport rate. In heat exchangers, coolers, and condensers, this condition is used to regulate heat transmission. The increased inertial force reduces fluid velocities and heat transfer, which may be desired to avoid overheating or meet thermal performance goals.

➢ The NF flow with aggregation shows enhanced heat transportation compared to the case without aggregation for increased Re values.

Nomenclature

T_∞	Ambient temperature	E	Constant torsional motion of the cylinder
C_{fx}, C_{fs}	Skin friction coefficients	Re	Reynolds number
Nu	Nusselt number	K	Positive constant
k	Thermal conductivity	ν	Kinematic viscosity
Q_0	Heat source/sink coefficient	T_w	Surface temperature
ϕ	Volume fraction	$f'(\eta), g(\eta)$	Dimensionless velocity profiles
a	Stretching strength	$\theta(\eta)$	Dimensionless thermal profile
Q	Heat source/sink parameter	μ	Dynamic viscosity
ϕ_{int}	Solid volume fraction of aggregates	ρC_p	Heat capacitance
Pr	Prandtl number	Subscripts	
(u, v, w)	Velocity components	f	Fluid
T	Temperature	agg	Aggregate
η	Dimensionless similarity coordinate	nf	Nanofluid
(r, φ, z)	Cylindrical coordinates	s	Solid nanoparticle
ρ	Density	bf	Base fluid

References

1. Wang, C.Y. Fluid flow due to a stretching cylinder. *Phys. Fluids* **1988**, *31*, 466. [CrossRef]
2. Sprague, M.A.; Weidman, P.D. Three-dimensional flow induced by the torsional motion of a cylinder. *Fluid Dyn. Res.* **2010**, *43*, 015501. [CrossRef]
3. Javed, M.F.; Khan, M.I.; Khan, N.B.; Muhammad, R.; Rehman, M.U.; Khan, S.W.; Khan, T.A. Axisymmetric flow of Casson fluid by a swirling cylinder. *Results Phys.* **2018**, *9*, 1250–1255. [CrossRef]
4. Khan, M.; Ahmed, A.; Ahmed, J. Boundary layer flow of Maxwell fluid due to torsional motion of cylinder: Modeling and simulation. *Appl. Math. Mech.* **2020**, *41*, 667–680. [CrossRef]
5. Ahmed, J.; Shahzad, A.; Farooq, A.; Kamran, M.; Khan, S.U.-D.; Khan, S.U.-D. Thermal analysis in swirling flow of titanium dioxide–aluminum oxide water hybrid nanofluid over a rotating cylinder. *J. Therm. Anal. Calorim.* **2020**, *144*, 2175–2185. [CrossRef]
6. Ali, A.M.; Rona, A.; Kadhim, H.T.; Angelino, M.; Gao, S. Thermo-hydraulic performance of a circular microchannel heat sink using swirl flow and nanofluid. *Appl. Therm. Eng.* **2021**, *191*, 116817. [CrossRef]
7. Rafiq, T.; Mustafa, M. Computational Analysis of Unsteady Swirling Flow Around a Decelerating Rotating Porous Disk in Nanofluid. *Arab. J. Sci. Eng.* **2019**, *45*, 1143–1154. [CrossRef]
8. Usman, A.H.; Khan, N.S.; Humphries, U.W.; Shah, Z.; Kumam, P.; Khan, W.; Khan, A.; Rano, S.A.; Ullah, Z. Development of Dynamic Model and Analytical Analysis for the Diffusion of Different Species in Non-Newtonian Nanofluid Swirling Flow. *Front. Phys.* **2021**, *8*, 616790. [CrossRef]
9. Reddy, P.S.; Sreedevi, P.; Chamkha, A.J. Heat and mass transfer analysis of nanofluid flow over swirling cylinder with Cattaneo–Christov heat flux. *J. Therm. Anal. Calorim.* **2021**, *147*, 3453–3468. [CrossRef]
10. Gangadhar, K.; Victoria, E.M.; Chamkha, A.J. Hydrothermal features in the swirling flow of radiated graphene—Fe_3O_4 hybrid nanofluids through a rotating cylinder with exponential space-dependent heat generation. *Waves Random Complex Media* **2022**, 1–24. [CrossRef]
11. Wensel, J.; Wright, B.; Thomas, D.; Douglas, W.; Mannhalter, B.; Cross, W.; Hong, H.; Kellar, J.J.; Smith, P.; Roy, W. Enhanced thermal conductivity by aggregation in heat transfer nanofluids containing metal oxide nanoparticles and carbon nanotubes. *Appl. Phys. Lett.* **2008**, *92*, 023110. [CrossRef]

12. Prasher, R.; Phelan, P.E.; Bhattacharya, P. Effect of Aggregation Kinetics on the Thermal Conductivity of Nanoscale Colloidal Solutions (Nanofluid). *Nano Lett.* **2006**, *6*, 1529–1534. [CrossRef]

13. Ellahi, R.; Hassan, M.; Zeeshan, A. Aggregation effects on water base Al$_2$O$_3$—Nanofluid over a permeable wedge in mixed convection. *Asia-Pac. J. Chem. Eng.* **2016**, *11*, 179–186. [CrossRef]

14. Zhou, L.; Zhu, J.; Zhao, Y.; Ma, H. A molecular dynamics study on thermal conductivity enhancement mechanism of nanofluids—Effect of nanoparticle aggregation. *Int. J. Heat Mass Transf.* **2021**, *183*, 122124. [CrossRef]

15. Roodbari, M.; Abbasi, M.; Arabha, S.; Gharedaghi, A.; Rajabpour, A. Interfacial thermal conductance between TiO2 nanoparticle and water: A molecular dynamics study. *J. Mol. Liq.* **2021**, *348*, 118053. [CrossRef]

16. Alzahrani, F.; Gowda, R.P.; Kumar, R.N.; Khan, M.I. Dynamics of thermosolutal Marangoni convection and nanoparticle aggregation effects on Oldroyd-B nanofluid past a porous boundary with homogeneous-heterogeneous catalytic reactions. *J. Indian Chem. Soc.* **2022**, *99*, 100458. [CrossRef]

17. Wang, F.; Kumar, R.N.; Prasannakumara, B.C.; Khan, U.; Zaib, A.; Abdel-Aty, A.-H.; Yahia, I.S.; Alqahtani, M.S.; Galal, A.M. Aspects of Uniform Horizontal Magnetic Field and Nanoparticle Aggregation in the Flow of Nanofluid with Melting Heat Transfer. *Nanomaterials* **2022**, *12*, 1000. [CrossRef]

18. Wang, F.; Rani, S.P.; Sarada, K.; Gowda, R.P.; Khan, U.; Zahran, H.Y.; Mahmoud, E.E. The effects of nanoparticle aggregation and radiation on the flow of nanofluid between the gap of a disk and cone. *Case Stud. Therm. Eng.* **2022**, *33*, 101930. [CrossRef]

19. Mahanthesh, B. Flow and heat transport of nanomaterial with quadratic radiative heat flux and aggregation kinematics of nanoparticles. *Int. Commun. Heat Mass Transf.* **2021**, *127*, 105521. [CrossRef]

20. Yu, Y.; Madhukesh, J.K.; Khan, U.; Zaib, A.; Abdel-Aty, A.-H.; Yahia, I.S.; Alqahtani, M.S.; Wang, F.; Galal, A.M. Nanoparticle Aggregation and Thermophoretic Particle Deposition Process in the Flow of Micropolar Nanofluid over a Stretching Sheet. *Nanomaterials* **2022**, *12*, 977. [CrossRef]

21. Muthucumaraswamy, R.; Sivakumar, P. MHD flow past a parabolic flow past an infinite isothermal vertical plate in the presence of thermal radiation and chemical reaction. *Int. J. Appl. Mech. Eng.* **2016**, *21*, 95–105. [CrossRef]

22. Radhika, M.; Gowda, R.J.P.; Naveenkumar, R.; Siddabasappa; Prasannakumara, B.C. Heat transfer in dusty fluid with suspended hybrid nanoparticles over a melting surface. *Heat Transf.* **2020**, *50*, 2150–2167. [CrossRef]

23. Faisal, M.; Ahmad, I.; Javed, T. Numerical simulation of mixed convective 3D flow of a chemically reactive nanofluid subject to convective Nield's conditions with a nonuniform heat source/sink. *Heat Transf.* **2020**, *50*, 352–369. [CrossRef]

24. Chu, Y.-M.; Nazeer, M.; Khan, M.I.; Hussain, F.; Rafi, H.; Qayyum, S.; Abdelmalek, Z. Combined impacts of heat source/sink, radiative heat flux, temperature dependent thermal conductivity on forced convective Rabinowitsch fluid. *Int. Commun. Heat Mass Transf.* **2020**, *120*, 105011. [CrossRef]

25. Punith Gowda, R.J.; Naveen Kumar, R.; Jyothi, A.M.; Prasannakumara, B.C.; Sarris, I.E. Impact of Binary Chemical Reaction and Activation Energy on Heat and Mass Transfer of Marangoni Driven Boundary Layer Flow of a Non-Newtonian Nanofluid. *Processes* **2021**, *9*, 702. [CrossRef]

26. Fang, T.; Yao, S. Viscous Swirling Flow over a Stretching Cylinder. *Chin. Phys. Lett.* **2011**, *28*, 114702. [CrossRef]

27. Acharya, N.; Das, K.; Kundu, P.K. Effects of aggregation kinetics on nanoscale colloidal solution inside a rotating channel. *J. Therm. Anal. Calorim.* **2019**, *138*, 461–477. [CrossRef]

28. Benos, L.; Karvelas, E.; Sarris, I. Crucial effect of aggregations in CNT-water nanofluid magnetohydrodynamic natural convection. *Therm. Sci. Eng. Prog.* **2019**, *11*, 263–271. [CrossRef]

29. Mackolil, J.; Mahanthesh, B. Sensitivity analysis of Marangoni convection in TiO$_2$–EG nanoliquid with nanoparticle aggregation and temperature-dependent surface tension. *J. Therm. Anal. Calorim.* **2020**, *143*, 2085–2098. [CrossRef]

30. Leela, V.; Prasannakumara, B.C.; Shilpa, B.; Reddy, R.G. Computational analysis of ohmic and viscous dissipation effects on MHD mixed convection flow in a vertical channel with linearly varying wall temperatures. *Proc. Inst. Mech. Eng. Part E J. Process. Mech. Eng.* **2022**. [CrossRef]

31. Rani, H.P.; Leela, V.; Shilpa, B.; Nagabhushana, P. Numerical analysis of hydromagnetic mixed convective flow in an internally heated vertical porous layer using thermal nonequilibrium model. *Heat Transf.* **2022**, *51*, 6249–6273. [CrossRef]

32. Shilpa, B.; Leela, V.; Rani, H.P. Stability analysis of MHD radiative mixed convective flow in vertical cylindrical annulus: Thermal nonequilibrium approach. *Heat Transf.* **2022**, *52*, 707–733. [CrossRef]

33. Leela, V.; Nagabhushana, P.; Shilpa, B.; Reddy, R.G. Numerical investigation on effects of induced magnetic field and viscous dissipation on MHD mixed convection in a vertical micro-porous channel using the Brinkman–Forchheimer extended Darcy model. *Int. J. Ambient. Energy* **2022**, *43*, 6950–6964. [CrossRef]

34. Shilpa, B.; Leela, V.; Prasannakumara, B.C.; Nagabhushana, P. Soret and Dufour effects on MHD double-diffusive mixed convective heat and mass transfer of couple stress fluid in a channel formed by electrically conducting and non-conducting walls. *Waves Random Complex Media* **2022**, 1–22. [CrossRef]